Superior plastic flow stability of self-patterned carbide - amorphous ceramic nanostructures

Wu, Wenqian
Shao, Lin
Li, Nan
Li, Lin
Wang, Jian

To be published in: Materials Research Letters

DOI to publisher's version: 10.1080/21663831.2025.2507314

Materials Research Letters

ISSN: 2166-3831 (Online) Journal homepage: www.tandfonline.com/journals/tmrl20

Superior plastic flow stability of self-patterned carbide – amorphous ceramic nanostructures

Wenqian Wu, Lin Shao, Nan Li, Lin Li & Jian Wang

To cite this article: Wenqian Wu, Lin Shao, Nan Li, Lin Li & Jian Wang (2025) Superior plastic flow stability of self-patterned carbide – amorphous ceramic nanostructures, Materials Research Letters, 13:7, 719-728, DOI: 10.1080/21663831.2025.2507314

To link to this article: https://doi.org/10.1080/21663831.2025.2507314

MATER. RES. LETT.
2025, VOL. 13, NO. 7, 719–728
https://doi.org/10.1080/21663831.2025.2507314

MATERIALS RESEARCH LETTERS
Taylor & Francis
Taylor & Francis Group

ORIGINAL REPORT

OPEN ACCESS Check for updates

Superior plastic flow stability of self-patterned carbide – amorphous ceramic nanostructures

Wenqian Wu[a], Lin Shao[b], Nan Li[c], Lin Li[d] and Jian Wang [a]

[a]Department of Mechanical and Materials Engineering, University of Nebraska-Lincoln, Lincoln, NE, USA; [b]Department of Nuclear Engineering, Texas A&M University, College Station, TX, USA; [c]MPA-CINT, Los Alamos National Laboratory, Los Alamos, NM, USA; [d]School for Engineering of Matter, Transport and Energy, Arizona State University, Tempe, AZ, USA

ABSTRACT

Amorphous ceramics and carbides exhibit superb strength but poor plasticity. Here, we synthesized TiC-SiOC nanostructures with TiC-nanocarbides embedded in amorphous ceramic SiOC by co-sputtering followed by high-temperature annealing and/or irradiation. TiC-SiOC nanostructures exhibit high strength and good plastic flow stability even after heavy irradiation, 7 GPa at room temperature and 3.6 GPa at 700 °C with a uniform strain of about 10% ~ 18%. The uniform deformation is accommodated by the shearing of amorphous ceramic and the rotation of nanocarbides. Nanocarbides inhibit the propagation of shear banding in amorphous SiOC, and amorphous-crystal interfaces act as sinks to manage irradiation-induced defects.

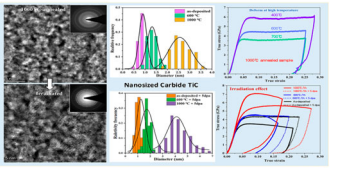

IMPACT STATEMENT

Amorphous ceramics and carbides exhibit superb strength but poor plasticity. Dual-phase heterogeneous nanostructures with nanocarbides self-patterned in nanosized amorphous ceramics exhibit ultra-high strength and plastic flow stability as well as retain highly stable microstructure under high temperature, irradiation, and mechanical loading.

ARTICLE HISTORY
Received 13 February 2025

KEYWORDS
Strength; plasticity; stability; irradiation; dual-phase nanostructure

1. Introduction

Structural materials with high-temperature strength, good plasticity, and microstructural stability are in high demand for applications in extreme environments, such as advanced nuclear reactors [1], airplane engines [2], hypersonic vehicles [3] and high frequency electromagnetic radiation [4,5]. Compared with metals and intermetallic, ceramics and carbides generally exhibit high strength but poor plasticity in a wide range of deformation temperature [6–8]. In addition, crystalline ceramics and carbides have the intrinsic issue of forming radiation-induced crystal defects (vacancies, interstitials and bubbles) [9–12]. The plasticity of polycrystalline carbide and ceramics could be accommodated by grain boundary sliding [13–15]. Nanocrystalline SiC with amorphous grain boundaries exhibits a crossover from intergranular continuous deformation to intragrain discrete deformation, endowing the brittle SiC ceramic with high fracture toughness [14]. However, grain coarsening and recrystallization of amorphous phase at high temperature will diminish the capability of grain boundary sliding [16,17]. Dual-phase metal-ceramic and metal-carbide nanolaminates exhibit measurable plasticity due to geometry constraint-promoted plasticity in carbide and ceramics [18–20], but the strength significantly decreases at high temperature due to the metal phase [21]. Moreover, lamellar structures cause anisotropic mechanical properties [22]. Although metallic glass-based crystal-amorphous nanocomposites have been reported to exhibit high strength and large plasticity,

CONTACT Jian Wang jianwang@unl.edu Department of Mechanical and Materials Engineering, University of Nebraska-Lincoln, Lincoln, NE 68588, USA

Supplemental data for this article can be accessed online at https://doi.org/10.1080/21663831.2025.2507314.

rapid recrystallization occurs in metallic glass under irradiation and heating conditions due to its low structure stability [23,24].

Three-dimensional crystalline carbide—amorphous ceramics nanostructures are expected to conquer mechanical anisotropy of lamellar structures, softening and low structure stability at high temperature. When such nanostructures deform, plastic flow localization may develop in amorphous regions, and crystalline carbides will impede individual flow-localized zones from extending across the entire length of the material [25–27]. In addition, amorphous ceramics display high-temperature thermal stability due to high melting temperature [28,29] and extreme radiation tolerance [30]. Amorphous-crystal interfaces can act as sinks and recombination centers for radiation-induced defects (interstitials and vacancies) in nanocrystals and for radiation-induced free volume (both positive and negative) in amorphous matrix [31,32]. The defect removal prevents phase changes and defect clustering.

Here, we synthesized carbide (TiC)—amorphous silicon oxycarbide (SiOC) nanostructures (referred to as TiC-SiOC) with a three-dimensional dual-phase nanostructure. Amorphous SiOC ceramic was chosen because of its high strength, excellent irradiation resistance and structure stability up to 1300 ℃ [30,33,34]. Ti was chosen because of its high bonding energy with non-metallic elements C and O [35,36], which contributes to high thermal stability and induces the in-situ formation of TiC nanocrystals under high temperatures and irradiation conditions. The characteristic microstructure enables the TiC-SiOC to exhibit ultra-high strength and plastic flow stability as well as retaining highly stable microstructure under high temperature and irradiation. Although the Ti/TiC-SiOC ceramic matrix composites have been reported based on active filler-controlled pyrolysis of polysiloxanes with Ti filter additions, the micron-scale characteristic microstructures usually induce catastrophic failure by shear banding/cracking in the amorphous matrix and interface decohesion [37].

2. Synthesis and characterizations

TiC-SiOC thin films were synthesized by co-sputtering Ti, SiC and SiO_2 targets onto a SiO_2/Si substrate, as illustrated in Figure S1a. The nominal composition is 20.1 at.% Ti, 22.8 at.% Si, 38.3 at.% O, and 18.8 at.% C (Figure S1b). The as-deposited samples were annealed at 600 and 1000 ℃ under Ar gas flow for 1 hour, respectively. Cu ion irradiation tests with energies (5, 4, 3, 2, 1 MeV) were performed on the as-deposited and annealed samples. By using the Stopping and Range of Ions in Matter (SRIM)−2013 software [38,39], the irradiation damages are uniformly distributed throughout the top 4 μm of thin film (Figure S1c) and less than 0.1 at.% Cu atoms are implanted (Figure S1d). No obvious surface change of the thin film was observed after irradiation (Figure S1e–f).

TiC-SiOC nanostructures were evaluated by in-situ SEM micropillar compression tests under a displacement-control mode at strain rate of 10^{-3} s^{-1}. Micropillars with a diameter of about 2 μm and aspect ratio (height/diameter) of 2 were prepared by focused ion beam (FIB). Elastic modulus and hardness were obtained by nanoindentation test [40]. Microstructure characterization was performed using transmission electron microscopy (TEM). Cross-sectional TEM samples were prepared by low energy Ar + ion milling and FIB lift-out technique. The details can be found in Supplementary information.

3. Results and discussion

The as-deposited sample exhibits a three-dimensional dual-phase nanostructure, as revealed by the typical amorphous halo in the diffraction pattern and local contrast variation in the HRSTEM image (Figure 1a). The uniformly distributed nanocrystals in amorphous matrix developed during both high temperature annealing and irradiation (Figure 1b–f). It is noted that irradiation promotes the growth of nanocrystals as evidenced by less lattice distortion and improved diffraction intensity after irradiation, which should be related to the thermal spike effect [41] and enhanced diffusivity by irradiation [42]. The average diameter of nanocrystals increases from 1.0 to 2.5 nm with increasing annealing temperature (Figure 1g) and from 1.0 to 4.5 nm with further irradiation (Figure 1h). Notably, the diameter of nanocrystals is less than 5 nm even after 1000 ℃ annealing and heavy irradiation, revealing structure stability of the nanostructures. The volume fraction of nanocrystals generally increases with annealing and irradiation (Figure 1i). However, the volume fraction of nanocrystals in the 1000 ℃-annealed sample decreases after irradiation, suggesting that 1000 ℃-annealing promotes the growth of nanocrystals, achieving a maximized content of crystalline phase. Further irradiation destroys nanocrystals to some extent and thickens amorphous interfaces. The diffraction pattern of 1000 ℃-annealed sample (Figure 1j) suggests that these nanocrystals have a face-centered cubic (fcc) structure. Figure 1k–l present the corresponding dark field imaging of nanocrystals in the 1000 ℃-annealed sample before and after irradiation, respectively. Apparently, irradiation promotes coarsening of nanocrystals and increases the thickness of amorphous interfaces.

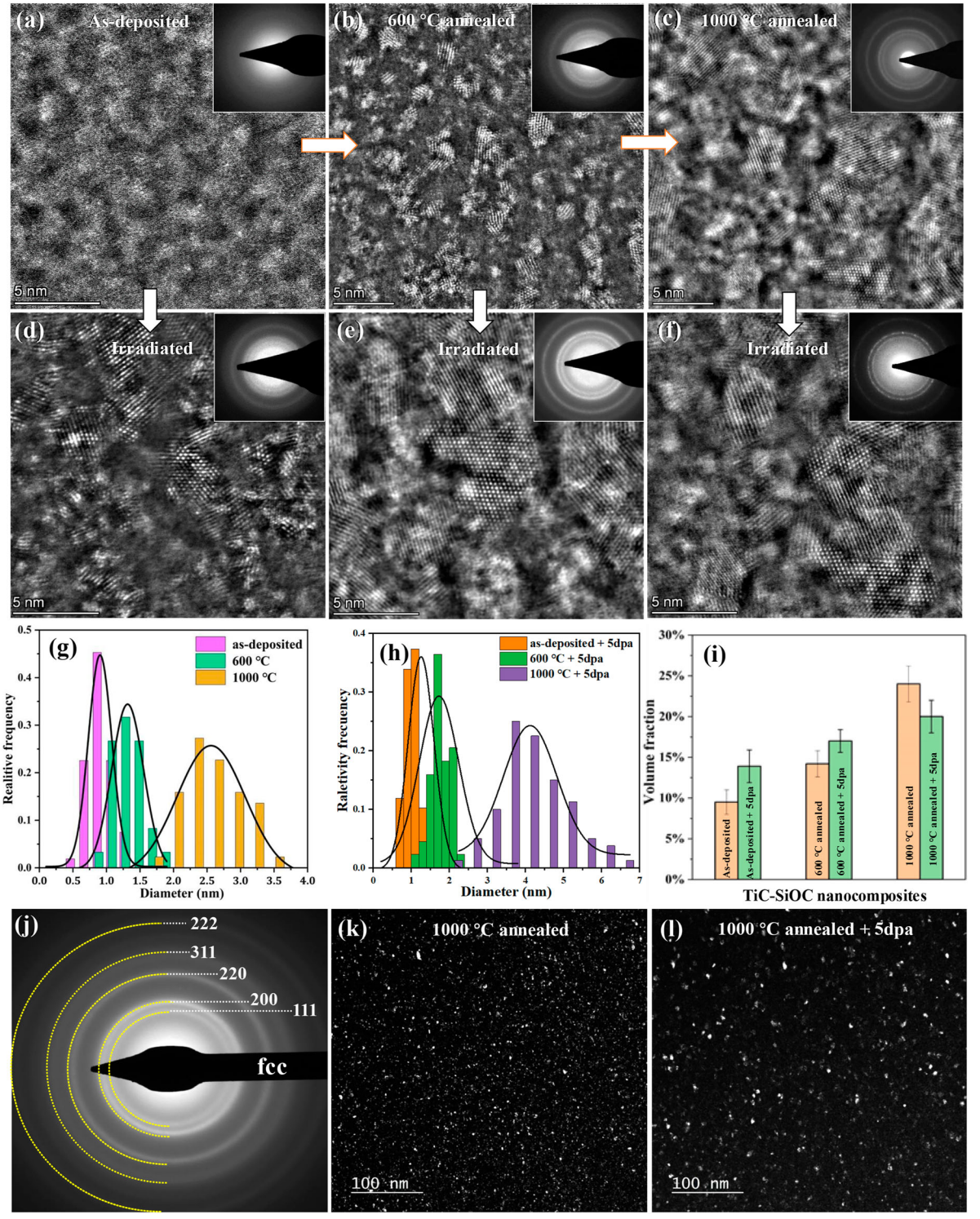

Figure 1. (a–f) HRSTEM images of TiC-SiOC nanostructures before and after ion irradiation: (a) as-deposited sample, (b) 600 °C-annealed sample, (c) 1000 °C-annealed sample, (d) as-deposited sample after irradiation, (e) 600 °C-annealed sample after irradiation, and (f) 1000 °C-annealed sample after irradiation; (g-i) Statistical analysis of the nanocrystals in TiC-SiOC nanostructures with different states: (g) feature size of nanocrystals after annealing, (h) feature size of nanocrystals after irradiation, (i) volume fraction of nanocrystals; (j) Representative electron diffraction pattern of the 1000 °C-annealed sample showing the typical fcc structure of nanocrystals; Dark field imaging of fcc nanocrystals in the 1000°C-annealed sample: (k) before and (l) after irradiation.

The element distributions of Ti-Si-O–C nanostructures were investigated by EDX HRSTEM-mapping. The heterogeneous amorphous structure of as-deposited sample is related to Ti-rich nanoclusters (Figure 2a). Based on bonding type analysis between metal and nonmetal elements [35,36], Ti will segregate during deposition under room temperature, promoting the formation of Ti-rich nanoclusters, as evidenced by the elemental mapping in Figure 2a. Compared to high temperature annealing (Figure 2b–c), irradiation promotes element separation as evidenced by obvious distribution of Ti and C in fcc nanocrystals and Si and O in amorphous matrix (Figure 2d–f). These nanocrystals with a fcc structure are rich with Ti and C elements after annealing and irradiation (Figure 2b–f). The 111 interplanar spacing measured from HRTEM images and corresponding lattice constant are 0.252 and 0.4365 nm, respectively (Figure S2). Thus, these nanocrystals are determined to be TiC carbides which exhibit a typical fcc structure with a lattice constant of 0.4326 nm [43]. Correspondingly, we refer this to TiC-SiOC dual-phase nanostructures with the nanocrystal carbides TiC and amorphous ceramics SiOC matrix. Note that the formation of TiC nano-carbides will induce a reduction of C content in the SiOC matrix. This is mainly related to irradiation-promoted bond breaking and reorganization [44]. Ion irradiation breaks the original Ti-Si-O–C bonds, and TiC nano-carbides are formed through the interaction of Ti nanoclusters and separated C atoms, due to their high electronegativity difference [45].

Figure 3a shows the true stress–strain curves at room temperature. In contrast to the brittle behavior or shear banding associated with catastrophic fracture in conventional amorphous ceramics, the as-deposited sample exhibits a yield strength of ~3.5 GPa and a uniform compressive strain of ~15%. High temperature annealing (600–1000 °C) monotonously enhances the yield/flow strength of TiC-SiOC nanostructures while maintaining good compressive plasticity. For example, the 1000 °C-annealed sample displays a yield strength of ~7.0 GPa and a uniform compressive strain of ~12%. In addition to densification of TiC-SiOC nanostructures, the enhanced yield/flow strength after annealing is mainly attributed to the formation of nanosized carbides TiC that possess an ultra-high shear modulus (~190 GPa) and hardness (~25 GPa) [46], i.e. higher volume fraction and the increased dimension of TiC nano-carbides. The corresponding SEM images of micropillars (Figure 3b1–b3) reveal plastic deformation behaviors. *In-situ* deformations were recorded in videos v1–v3. Small cracks (indicated by yellow arrows) were produced on the as-deposited and 600 °C-annealed micropillar surfaces, which leads to softening behavior at the later deformation stage in Figure 3a. In contrast, the 1000 °C-annealed sample exhibits superb mechanical properties in a wide range of deformation temperatures. At room temperature, the 1000 °C-annealed micropillar exhibits multiple thin shear bands (marked by a red arrow in Figure 3b3) without cracking or obvious strain localization. Furthermore, we tested 1000 °C-annealed samples at high temperature of 400, 600 and 700 °C, respectively. The true stress–strain curves in Figure 3c reveal that the yield/flow strength is maintained as high as 6.0 GPa at 400°C, 4.5 GPa at 600 °C, and 3.6 GPa at 700 °C, respectively. Figure 3d1–d3 present the corresponding SEM of micropillars. *In-situ* deformations were recorded in videos v4-v6. No cracks were observed during testing even the compressive strain is higher than 20%. Multiple shear bandings were observed when compression at 400 °C but not at 600 and 700 °C. Alternatively, uniform plastic deformation was observed at 600 and 700 °C. The improved plasticity is mainly attributed to the enhanced viscoplastic flow ability of the amorphous matrix with increasing temperature [47,48]. Compared to other typical irradiation-resistant materials [26,27,33,49–54], TiC-SiOC dual-phase nanostructures exhibit ultrahigh strength and good plasticity (Figure S3).

Microstructure characterizations revealed that irradiation promotes the growth of nanocrystal carbides in as-deposited TiC-SiOC nanostructures. In addition, irradiation changes the composition of amorphous ceramics, softening amorphous SiOC while enhancing its plastic flow ability. The structure unit of amorphous SiOC is generally referred to SiO_xC_{4-x} (x = 1,2,3,4), which can be considered as a C-doped amorphous SiO_2 with SiO_4 tetrahedra unit [55]. Si–C bonds can induce a tighter, more closely packed structure, contributing to higher elastic modulus, hardness, and significantly increased viscosity of SiOC ceramic [56,57]. Amorphous SiO_2 is reported to exhibit good plasticity since their SiO_4 tetrahedral unit can be easily tilted by bonds switching events which accommodate local strain in SiO_2 [58]. The reduced C content in SiOC matrix induced by the formation and growth of TiC carbides after irradiation will thus decrease the strength while improving the plasticity of the amorphous ceramic matrix. Therefore, the irradiated as-deposited sample shows both improved elastic modulus (Figure S4), strength and plasticity (Figure 4a). The yield strength increases from 3.5 to 4.3 GPa. More importantly, the irradiated sample exhibits uniform plastic deformation without cracking or shear banding after irradiation (Figure 4b1). The enhanced strength is attributed to the formation of irradiation-induced nano-carbides TiC. The *in-situ* deformations of TiC-SiOC nanostructures after irradiation were recorded in videos v7-v9. For the 600 °C-annealed TiC-SiOC nanostructures, the

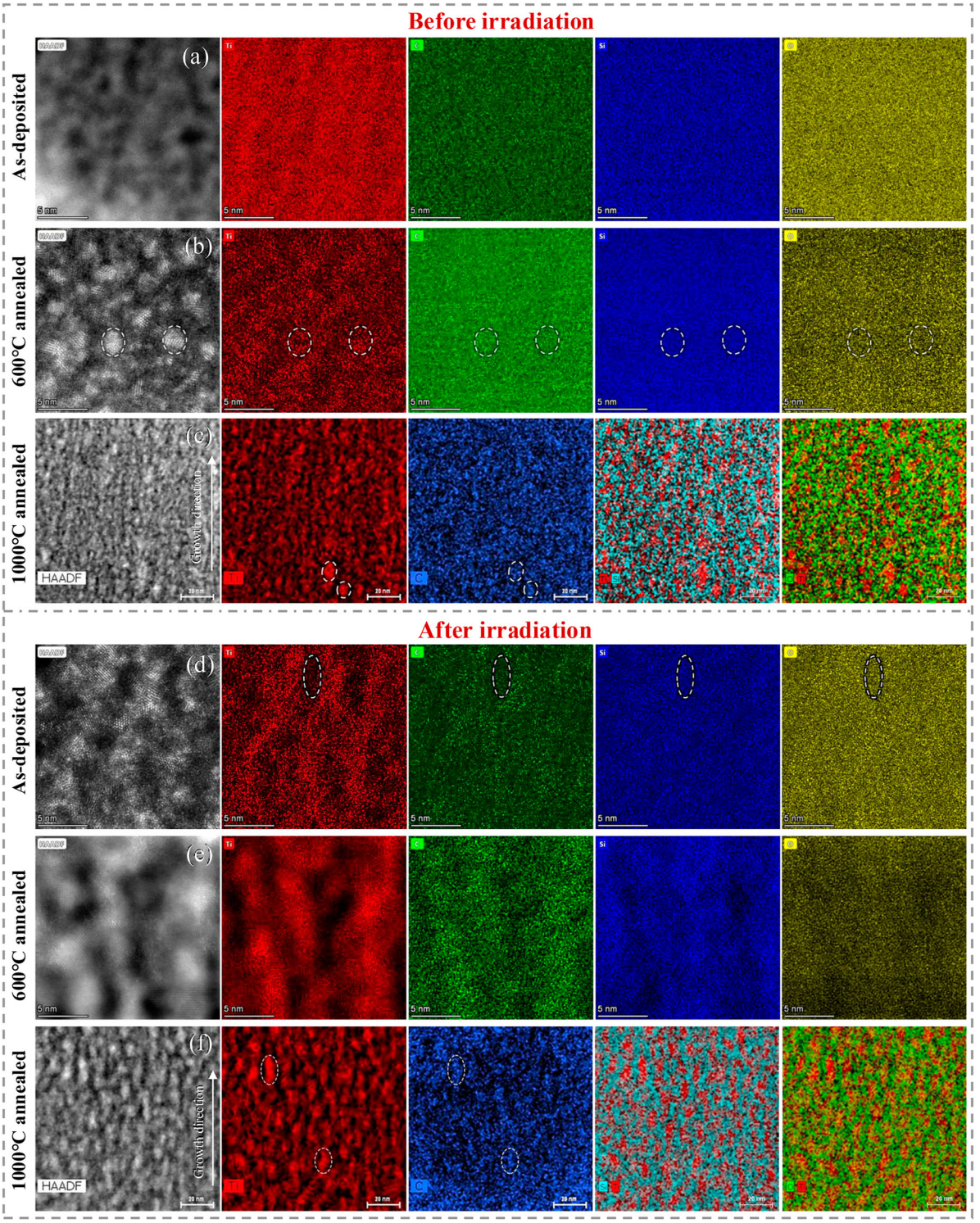

Figure 2. EDX-STEM mapping of TiC-SiOC nanostructures before and after ion irradiation: (a) as-deposited sample, (b) 600 °C-annealed sample, (c) 1000 °C-annealed sample; (d) as-deposited sample after irradiation, (e) 600 °C-annealed sample after irradiation, and (f) 1000 °C-annealed sample after irradiation.

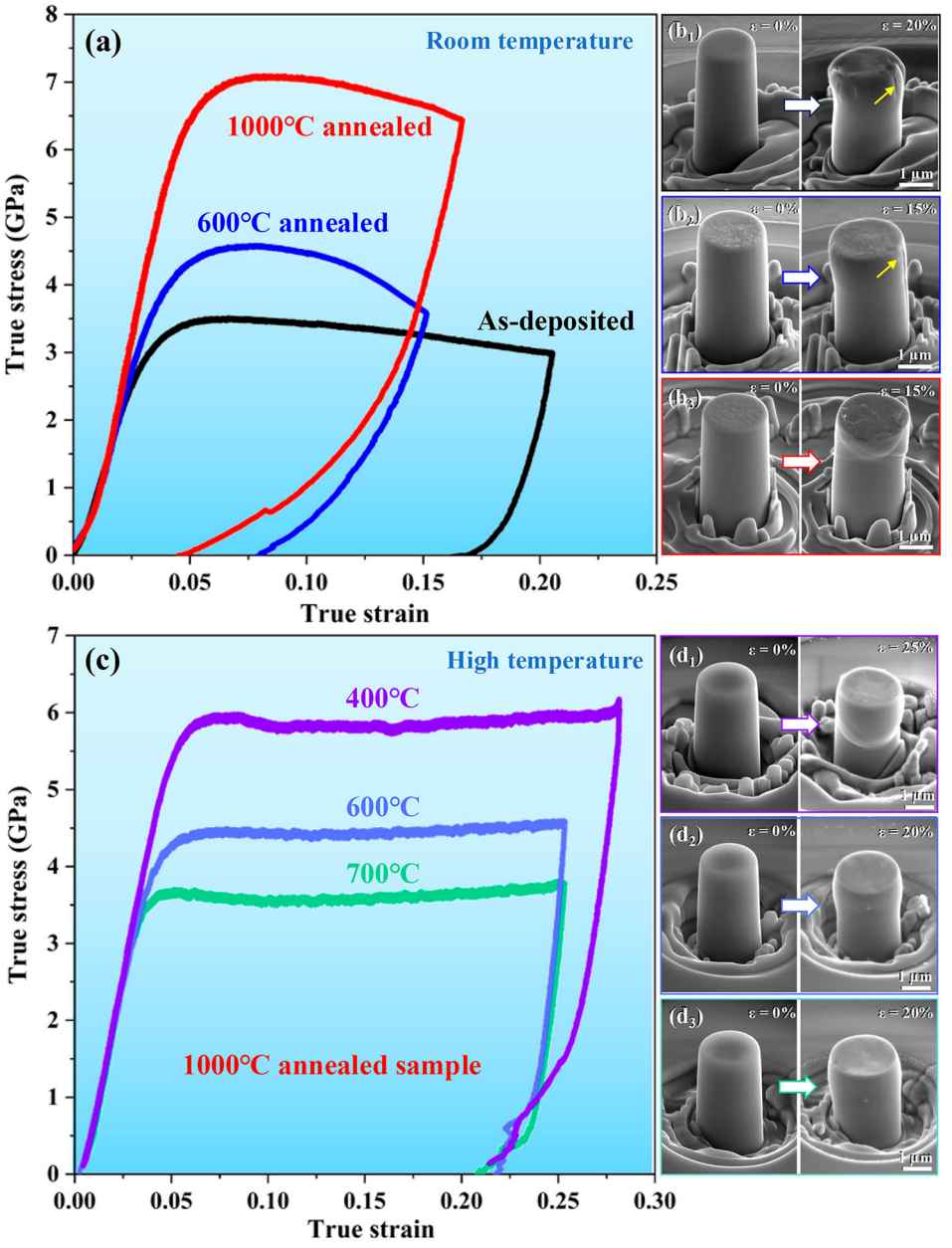

Figure 3. (a) Room temperature true stress-strain curves of the as-deposited and annealed TiC-SiOC nanostructures; (b1-b3) corresponding SEM images of micropillars before and after deformation at room temperature: (b1) as-deposited sample, (b2) 600 °C-annealed sample, (b3) 1000 °C-annealed sample; (c) High temperature true stress-strain curves of the 1000 °C-annealed TiC-SiOC nanostructure; (d1-d3) Corresponding SEM images of micropillars before and after deformation at high temperature: (d1) deformation under 400 °C, (d2) deformation under 600 °C and (d3) deformation under 700 °C.

yield strength remains at 4.5 GPa after irradiation (Figure 4a), while irradiation extensively enhances the uniform deformation capability from 10% to 18% (Figure 4b2). Therefore, the unchanged yield strength after irradiation could be attributed to the balance between strengthening effect by slightly increased volume fraction of TiC nano-carbides (Figure 1i) and softening effect by enhanced element separation (Figure 2e) after irradiation. The improved uniform deformation capability by irradiation can be attributed to three aspects: uniform distribution of TiC nano-carbides, reduced C content in amorphous SiOC ceramic matrix, and densification of nanostructures by incident high energy projectiles and corresponding enhanced diffusion by irradiation (Figure S5). However, for the 1000 °C-annealed TiC-SiOC nanostructure, irradiation causes the growth of nano-carbides but reduces the volume fraction of nano-carbides, the yield strength of the 1000 °C-annealed pillar thus decreases from 7.0 GPa to 5.5 GPa after irradiation (Figure 4a), while the uniform deformation capability

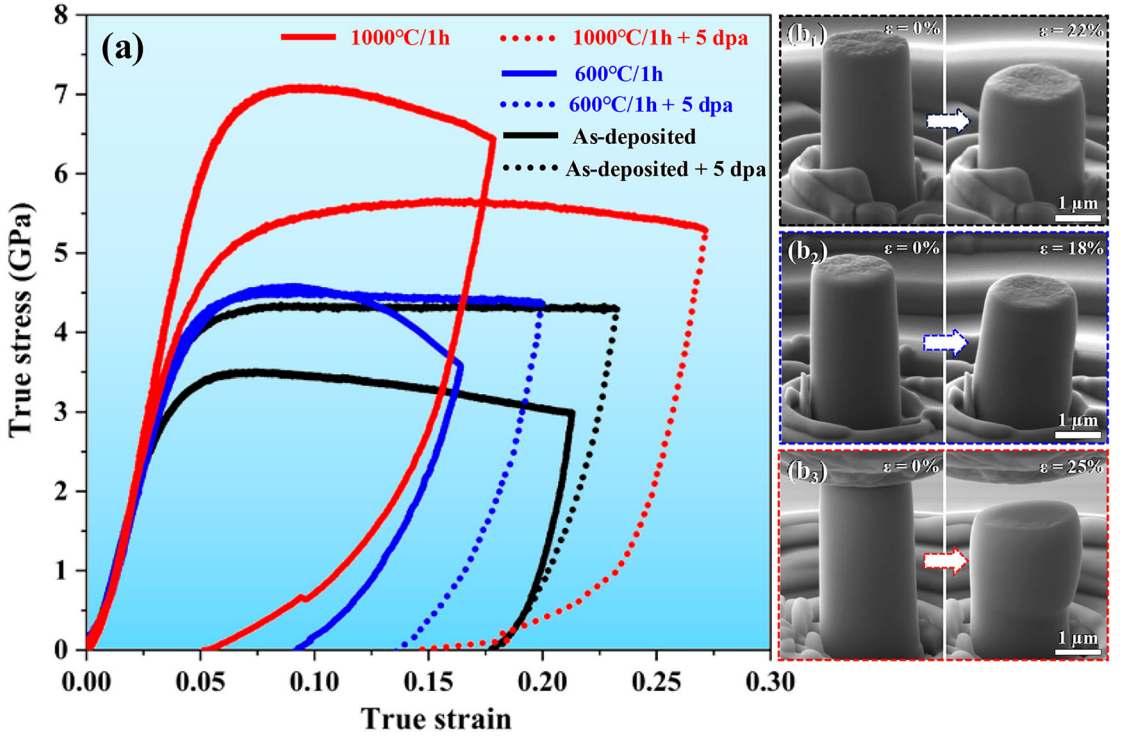

Figure 4. (a) Room temperature true stress-strain curves of the TiC-SiOC nanostructures after irradiation; (b1-b3) Corresponding SEM images of micropillars before and after deformation: (b1) as-deposited sample after irradiation, (b2) 600 °C-annealed sample after irradiation and (b3) 1000 °C-annealed sample after irradiation.

is extensively enhanced from 12% up to 25% (Figure 4b3). The decreased strength of the 1000 °C-annealed sample after irradiation could be ascribed to two factors: decreased volume fraction of TiC nano-carbides and softening effect of amorphous matrix SiOC due to reduced C element by irradiation promoted element separation (Figure 2f).

Improved plastic flow stability is related to microstructure-enabled deformation mechanisms. Figure 5a shows the cross-sectional STEM image of 1000 °C-annealed micropillar after compression, in which multiple nanoscale shear bands (marked by the red arrows) associated with small shear offsets on the micropillar surface were observed. These multiple ultrafine shear bands are supposed to contribute to good plasticity. Figure 5b presents the enlarged TEM image of the deformed microstructure and corresponding diffraction pattern. It is observed that the as-deposited and annealed samples have a nanocolumnar structure. Besides shear banding across multiple nanocolumns that formed during deposition, nanocolumns also bend to contribute compressive plasticity as marked by white dashed lines in Figure 5c and observed in corresponding *in-situ* deformation (video v3). It is also noted that diffraction pattern reveals no phase transformation during deformation (inset in Figure 5b) and the comparison of EDX STEM-mapping before and after deformation suggests rotation of TiC nano-carbides inside the shear band (Figure S6). Thus, the plastic flow ability should be enabled by the high-density TiC nano-carbides that act as strong barriers to the propagation of shear bands.

Compared with the 1000 °C-annealed Ti-SiOC, the irradiated 1000 °C-annealed Ti-SiOC exhibits significant enhancement of plastic flow stability. A cross-sectional TEM image of the micropillar shows that deformation was mainly accommodated in the irradiated section (Figure 5d). This verifies that irradiation causes the decreased strength while improving plasticity. Enlarged TEM (Figure 5e) and STEM images (Figure 5f) reveal that there is no obvious shape and feature size change of TiC nano-carbides after deformation, implying that TiC nano-carbides should accommodate plastic deformation by rotation due to its much higher strength than the amorphous matrix. The comparison of EDX STEM-mapping before and after deformation (Figure S7) clearly shows the rotation of TiC nano-carbides based on their near elliptical shape. Figure 5g1–g2 present two representative HRTEM images of TiC nano-carbides after deformation, which show perfect fcc structure without lattice defects. The rotation of TiC nano-carbides under compression should be ascribed to their dispersed distribution and softening effect of the amorphous ceramic matrix due to irradiation promoted element separation. Therefore, the carrier of plastic deformation in

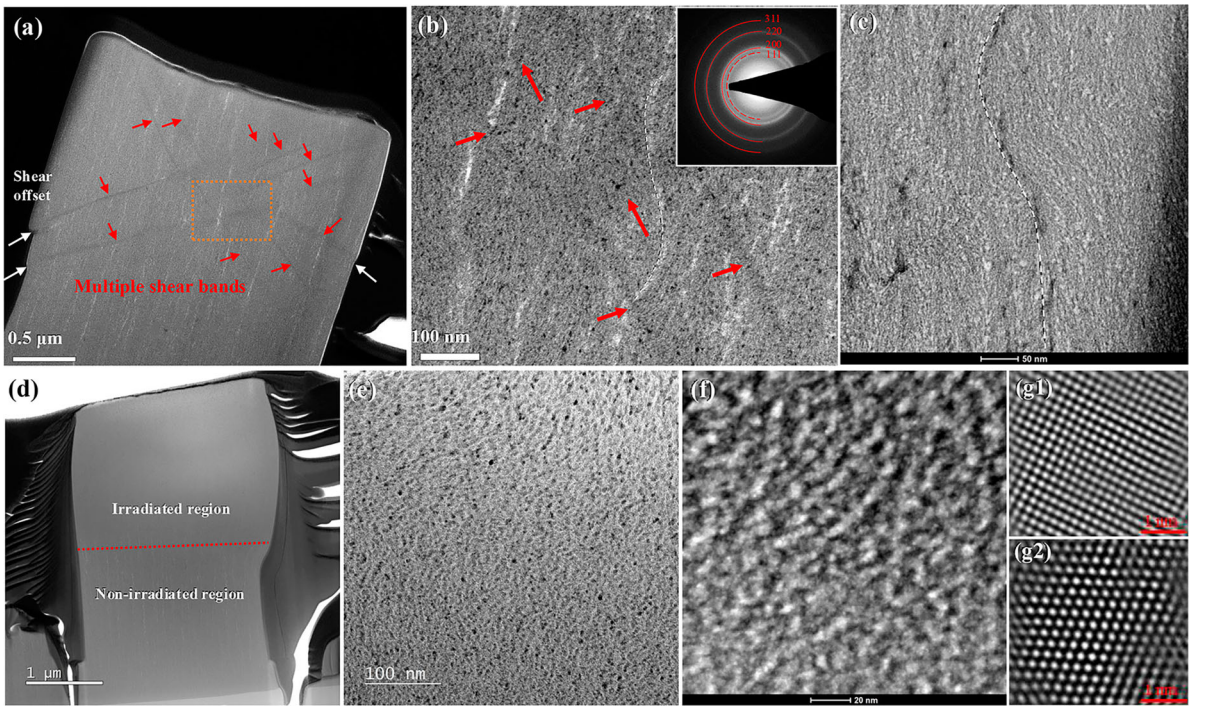

Figure 5. Microstructures of the room temperature deformed 1000 °C-annealed TiC-SiOC nanostructure before and after irradiation. (a) Cross-sectional TEM image of the deformed micropillar before irradiation; (b) TEM image and corresponding diffraction pattern of the deformed microstructure before irradiation; (c) STEM image of the deformed microstructure before irradiation; (d) Cross-sectional TEM image of the deformed micropillar after irradiation; (e) TEM image of the deformed microstructure after irradiation; (f) STEM image of the deformed microstructure after irradiation; (g1-g2) representative HRTEM images of TiC nanocrystals after deformation.

amorphous materials is accomplished by shear transformation zones (STZs) [59,60]. The shear instability associated with the formation and propagation of shear banding is ascribed to statistically occurring, spatially homogeneous nucleation of STZs and their coalescence. The high density of TiC nano-carbides with uniform distribution can thus divide the amorphous matrix into nanoscale, discretizing STZs and preventing the coalescence of STZs and formation/propagation of shear banding. Additionally, irradiation delaminates the nanocolumnar structure, eliminating the column bending-induced geometry instability.

4. Conclusion

The characteristic dual-phase nanostructures—nanosized metal carbides self-patterned in nanosized amorphous ceramics—exhibit ultra-high strength and plastic flow stability as well as retain highly stable microstructure under high temperature, irradiation, and mechanical loading. The mechanical properties of TiC-SiOC nanostructures are dominated by the volume fraction and distribution of TiC nano-carbides and the composition of amorphous ceramic matrix. The synergism between the shearing of amorphous ceramic boundaries and the rotation of nanosized carbides accommodate the enhanced plasticity of the nanostructures. The three-dimensional distributed TiC nanocrystals inhibit the fast propagation of shear banding in amorphous ceramics, enhancing plastic flow stability. In addition, amorphous domains and crystal-amorphous interfaces can be sinks for irradiation-induced defects, contributing to irradiation resistance. Such carbide-amorphous ceramic nanostructures, with a specifically designed ratio and composition of crystalline and amorphous phases, can be widely used as wear-resistant coatings and cladding materials in molten salt reactors. This work demonstrated a strategy to develop high strength, large plasticity, good thermal stability and irradiation tolerance of structural materials via composition and microstructure engineering.

Acknowledgements

The research was supported by the US National Science Foundation (NSF) (2132336/2331482). Synthesis and characterization were conducted at the Nebraska Center for Materials and Nanoscience (NCMN) and Nano-Engineering Research Core Facility (NERcF). High-temperature compression testing was performed at the Center for Integrated Nanotechnologies, Los Alamos National Laboratory, which is managed by Triad National Security, LLC for the U.S. Department of Energy's NNSA, under contract 89233218CNA000001.

Disclosure statement

No potential conflict of interest was reported by the author(s).

Funding

This work was supported by National Science Foundation: [Grant Number].

Author statement

Wu synthesized materials and performed in situ micro-mechanical tests and TEM characterization; Shao performed the ion irradiation test; Li (LANL) performed the high-temperature compression test. Wu and Wang prepared the manuscript. Wang and Li (ASU) conceived this study. All authors commented on the manuscript.

Declaration of competing interest

The authors declare that they have no known competing financial interests or personal relationships that could have appeared to influence the work reported in this paper.

ORCID

Jian Wang http://orcid.org/0000-0001-5130-300X

References

[1] Eswarappa Prameela S, Pollock TM, Raabe D, et al. Materials for extreme environments. Nat Rev Mater. 2023;8(2):81–88.
[2] Shahar FS, Sultan MTH. An overview of aerospace materials. Aerospace Materials. 2025: 3–40.
[3] Peters AB, Zhang D, Chen S, et al. Materials design for hypersonics. Nat Commun. 2024;15(1):3328.
[4] Duan S, Zhu D, Zhou W, et al. Mechanical and microwave absorption properties of Ti-filled SiCf/SiC composites via precursor infiltration and pyrolysis. J Mater Sci: Mater Electron. 2020;31(3):2634–2642.
[5] Yin X, Kong L, Zhang L, et al. Electromagnetic properties of Si–C–N based ceramics and composites. Int Mater Rev. 2014;59(6):326–355.
[6] Porz L. 60 years of dislocations in ceramics: A conceptual framework for dislocation mechanics in ceramics. Int J Ceram Eng Sci. 2022;4(4):214–239.
[7] Wiederhorn S. Brittle fracture and toughening mechanisms in ceramics. Annu Rev Mater Sci. 1984;14(1): 373–403.
[8] Xue K, Niu L-S, Shi H-J. Mechanical properties of amorphous silicon carbide. In: Mukherjee M, editor. Silicon-Carbide - Materials, Processing and Applications in Electronic Devices. 2011. InTech; 2011. p. 4-22. ISBN:978-953-307-968-4.
[9] Snead LL, Hay JC. Neutron irradiation induced amorphization of silicon carbide. J Nucl Mater. 1999;273(2): 213–220.
[10] Trinh L, Wang F, Bawane K, et al. Compositionally complex carbide ceramics: A perspective on irradiation damage. J Appl Phys. 2024;135(20):200901.
[11] Daghbouj N, Li BS, Callisti M, et al. Microstructural evolution of helium-irradiated 6H–SiC subjected to different irradiation conditions and annealing temperatures: A multiple characterization study. Acta Mater. 2019;181:160–172.
[12] Wang Z, Zhang L, AlMotasem AT, et al. Exploring defect behavior in helium-irradiated single-crystal and nanocrystalline 3C-SiC at 800°C: A synergy of experimental and simulation techniques. Acta Mater. 2024;279:120281.
[13] Karch J, Birringer R, Gleiter H. Ceramics ductile at low temperature. Nature. 1987;330(6148):556–558.
[14] Szlufarska I, Nakano A, Vashishta P. A Crossover in the Mechanical Response of Nanocrystalline Ceramics. Science. 2005;309(5736):911–914.
[15] Zhang JY, Sha ZD, Branicio PS, et al. Superplastic nanocrystalline ceramics at room temperature and high strain rates. Scr Mater. 2013;69(7):525–528.
[16] Castro RHR. On the thermodynamic stability of nanocrystalline ceramics. Mater Lett. 2013;96:45–56.
[17] Chiang YM, Smyth IP, Terwilliger CD, et al. (1990). Measurements of grain boundary properties in nanocrystalline ceramics.
[18] Yang W, Ayoub G, Salehinia I, et al. Deformation mechanisms in Ti/TiN multilayer under compressive loading. Acta Mater. 2017;122:99–108.
[19] Yang LW, Mayer C, Chawla N, et al. Deformation mechanisms of ultra-thin Al layers in Al/SiC nanolaminates as a function of thickness and temperature. Philos Mag. 2016;96(32-34):3336–3355.
[20] Supakul S, Jain M, Yaddanapudi K, et al. Synthesis, microstructure and micro-mechanical characterization of metal (Nb, Ti)-MAX phase (Ti2AlC) nanolaminates. Mater Sci Eng A. 2024;910:146905.
[21] Lotfian S, Rodríguez M, Yazzie KE, et al. High temperature micropillar compression of Al/SiC nanolaminates. Acta Mater. 2013;61(12):4439–4451.
[22] Qi Z, Zhu Q, Wang J, et al. Revealing interface-assisted plastic anisotropy via in situ transmission electron microscopy tension of lamellar TiAl. Sci China Mater. 2023;66(11):4275–4284.
[23] Li FC, Liu T, Zhang JY, et al. Amorphous–nanocrystalline alloys: fabrication, properties, and applications. Mater Today Adv. 2019;4:100027.
[24] Fu EG, Carter J, Martin M, et al. Ar-ion-milling-induced structural changes of Cu50Zr45Ti5 metallic glass. Nucl Instrum Methods Phys Res B. 2010;268(6):545–549.
[25] Ming K, Zhu Z, Zhu W, et al. Enhancing strength and ductility via crystalline-amorphous nanoarchitectures in TiZr-based alloys. Sci Adv. 2022;8(10):eabm 2884.
[26] Ming K, Gu C, Su Q, et al. Strength and plasticity of amorphous ceramics with self-patterned nano-heterogeneities. Int J Plast. 2020;134:102837.
[27] Wei B, Wu W, Nastasi M, et al. Plastic flow behaviors of high-strength dual-phase Ni-SiOC nanocomposites. Int J Plast. 2022;158:103431.
[28] Barsoum M. (2019). Fundamentals of ceramics.
[29] Fahrenholtz WG, Hilmas GE. Ultra-high temperature ceramics: Materials for extreme environments. Scr Mater. 2017;129:94–99.

[30] Nastasi M, Su Q, Price L, et al. Superior radiation tolerant materials: Amorphous silicon oxycarbide. J Nucl Mater. 2015;461:200–205.
[31] Wei B, Wu W, Wang J. In-Situ TEM Investigation of Helium Implantation in Ni-SiOC Nanocomposites. Materials (Basel). 2023;16(4):1357.
[32] Ludy JE, Rupert TJ. Amorphous intergranular films act as ultra-efficient point defect sinks during collision cascades. Scr Mater. 2016;110:37–40.
[33] Ming K, Gu C, Su Q, et al. Strength and plasticity of amorphous silicon oxycarbide. J Nucl Mater. 2019;516:289–296.
[34] Sorarù GD, Suttor D. High Temperature Stability of Sol-Gel-Derived SiOC Glasses. J Sol-Gel Sci Technol. 1999;14(1):69–74.
[35] Luo Y-R. (2007). Comprehensive handbook of chemical bond energies.
[36] Sanderson R. (2012). Chemical bonds and bonds energy.
[37] Akkaş HD, Öveçoğlu ML, Tanoğlu M. Silicon oxycarbide-based composites produced from pyrolysis of polysiloxanes with active Ti filler. J Eur Ceram Soc. 2006;26(15):3441–3449.
[38] Weber WJ, Zhang Y. Predicting damage production in monoatomic and multi-elemental targets using stopping and range of ions in matter code: Challenges and recommendations. Curr Opin Solid State Mater Sci. 2019;23(4):100757.
[39] Ziegler JF. (2012). Ion implantation science and technology.
[40] Oliver WC, Pharr GM. An improved technique for determining hardness and elastic modulus using load and displacement sensing indentation experiments. J Mater Res. 1992;7(6):1564–1583.
[41] Toulemonde M, Dufour C, Meftah A, et al. Transient thermal processes in heavy ion irradiation of crystalline inorganic insulators. Nucl Instrum Methods Phys Res Sect B Beam Interact Mater At. 2000;166-167:903–912.
[42] Starostin VA. A review of radiation enhanced diffusion in perspective materials. Nucl Instrum Methods Phys Res Sect B Beam Interact Mater At. 2006;242(1):402–405.
[43] Ingold JH. Thermionic Properties of Some Refractory Metal Carbides. J Appl Phys. 1963;34(7):2033–2039.
[44] Nastasi M, Mayer JW, Hirvonen JK. Ion-solid interactions: fundamentals and applications. city: Cambridge University Press; 1996.
[45] Sanderson RT. Electronegativity and bonding of transitional elements. Inorg Chem. 1986;25(19):3518–3522.
[46] Babapoor A, Asl MS, Ahmadi Z, et al. Effects of spark plasma sintering temperature on densification, hardness and thermal conductivity of titanium carbide. Ceram Int. 2018;44(12):14541–14546.
[47] Cheng S. Viscosity-temperature relation based on the evolution of medium-range structures of silica. J Non-Cryst Solids. 2021;557:120582.
[48] Rouxel T, Massouras G, Sorarù G-D. High Temperature Behavior of a Gel-Derived SiOC Glass: Elasticity and Viscosity. J Solgel Sci Technol. 1999;14(1):87–94.
[49] Bae S-G, Kim S, Lee J-A, et al. Improving the mechanical properties of amorphous silicon carbide fibers by forming a protective silicon dioxide layer. Ceram Int. 2022;48(20):30745–30753.
[50] Bai B, Han X, Zheng Q, et al. Composition optimization of high strength and ductility ODS alloy based on machine learning. Fusion Eng Des. 2020;161:111939.
[51] Deng L, Luo J-r, Tu J, et al. Achieving excellent mechanical properties of ODS steel by Y2O3 addition. Mater Sci Eng A. 2023;872:145008.
[52] Beyerlein IJ, Caro A, Demkowicz MJ, et al. Radiation damage tolerant nanomaterials. Mater Today. 2013;16(11):443–449.
[53] Wang Y, Li J, Hamza AV, et al. Ductile crystalline–amorphous nanolaminates. Proc Natl Acad Sci. 2007;104(27):11155–11160.
[54] Bai L, Wei B, Wang J, et al. High strength and thermal stability of core-shell Fe-SiOC nanocolumnar composites. Scr Mater. 2022;219:114885.
[55] Ding H, Demkowicz MJ. Hydrogen reverses the clustering tendency of carbon in amorphous silicon oxycarbide. Sci Rep. 2015;5(1):13051.
[56] Ionescu E, Balan C, Kleebe H-J, et al. High-Temperature Creep Behavior of Glass-Ceramics: Influence of Network Carbon Versus Segregated Carbon. J Am Ceram Soc. 2014;97(12):3935–3942.
[57] Rouxel T. Elastic Properties and Short-to Medium-Range Order in Glasses. J Am Ceram Soc. 2007;90(10):3019–3039.
[58] Luo J, Wang J, Bitzek E, et al. Size-Dependent Brittle-to-Ductile Transition in Silica Glass Nanofibers. Nano Lett. 2016;16(1):105–113.
[59] Langer JS. Shear-transformation-zone theory of deformation in metallic glasses. Scr Mater. 2006;54(3):375–379.
[60] Li L, Homer ER, Schuh CA. Shear transformation zone dynamics model for metallic glasses incorporating free volume as a state variable. Acta Mater. 2013;61(9):3347–3359.